

Doping effect on the magnetic and structural properties of $\text{Zn}_{0.97}\text{R}_{0.03}\text{O}$ ($R = \text{Li, Mg, Cr, Mn, Fe and Cd}$)

Tarob A. Abdel-Baset¹, Arnab Majumdar^{2*}, Rajeev Ahuja², Alexander N. Vasiliev^{3,4,5},
Mahmoud Abdel-Hafiez^{2,6,7}

¹Faculty of Science, Department of Physics, Fayoum University, Fayoum, Egypt.

²Department of Physics and Astronomy, Uppsala University, Uppsala, 75120, Sweden.

³Moscow State University, Moscow 119991, Russia

⁴South Ural State University, Chelyabinsk 454080, Russia

⁵Ural Federal University, 620002 Ekaterinburg, Russia

⁶National University of Science and Technology “MISiS”, Moscow 119049, Russia

⁷Lyman Laboratory of Physics, Harvard University, Cambridge, Massachusetts 02138, USA.

*arnab.majumdar@physics.uu.se

Abstract

Nonmagnetic ZnO has the potential for spintronic applications if doped with 1% to 10% of magnetic transition-metal (R) ions (Mn, Cr, Co, Fe, *etc.*). Zinc oxide is an extensively studied metal oxide semiconductor due to its myriad properties. It has a direct energy band gap of approximately ~ 3.4 eV at room temperature. The influence of doping in $\text{Zn}_{0.97}\text{R}_{0.03}\text{O}$ ($R = \text{Li, Mg, Cr, Mn, Fe and Cd}$) on the electronic, structural, and magnetic properties of ZnO has been investigated in this work. The exact compositions of the samples that were prepared were determined from the field emission scanning electron microscope. X-ray diffraction of the samples confirmed that they possessed single-phase hexagonal wurtzite crystal structure. Introducing Cr, Mn and Fe along with Mg into ZnO induces a clear magnetic moment without any apparent distortion in the structural morphology. The spatial configuration of dopant atoms is determined from first-principles, giving a better understanding of the position of the dopant atom responsible for the magnetism.

Introduction

The manifestation of magnetism in semiconductors has brought about the research for next generation magnetic semiconductors. In these materials, rather than the electron charge, it is the electron spin that carries information¹. These diluted magnetic semiconductors (DMSs) are formed when the cations in a non-magnetic semiconductor are partially replaced by magnetic transition metal ions²⁻⁵. They have garnered considerable interest as they possess the potential for interesting and practical applications in fields such as spintronics, spin-valve transistors, spin light-emitting diodes, and logic devices^{6,7}. One such DMS, is the transition metal (TM) doped ZnO which has attracted a lot of concern. This is due to their unprecedented potential applications in the field of spintronic devices¹⁻⁸. Wurtzite ZnO has a direct band gap (E_g) of about 3.4 eV and high exciton binding energy of 60 meV. It also shows piezoelectricity, and high thermal and chemical stability with respect to the environment⁹⁻¹³. The electron Hall mobility ($\sim 200 \text{ cm}^2 \text{ Vs}^{-1}$) and Curie temperature for doped ZnO are also quite high. These qualities render ZnO a material of paramount significance for a variety of optoelectronic and electronic applications¹⁴. Depending on the method of preparation, TM doping in the identical host lattice of ZnO can yield both paramagnetism as well as ferromagnetism¹⁵⁻¹⁷. ZnO nanoparticles can be synthesized by different methods. These methods include physical vapor phase deposition¹⁸, metal organic chemical vapor deposition¹⁹, and low temperature hydrothermal method²⁰.

The fundamental reason behind the origin of ferromagnetism in TM doped ZnO is still not fully understood. Different models have been put forward to explain the mechanism for the ferromagnetism at room temperature in DMSs. These explanations include interaction between bound magnetic polarons²¹, charge transfer ferromagnetism model^{22,23}, oxygen and zinc vacancies, V_O and V_{Zn} , interstitials, O_i and Zn_i , surfaces and grain boundaries, *etc.*²⁴⁻³⁰. The possibility of observing ferromagnetism in ZnO-based systems on being doped with nonmagnetic atoms like carbon³¹ or nitrogen³² has paved

the way for further research. This type of magnetism is known as d^0 ferromagnetism³³ and has been experimentally observed in ZnO-based systems prepared by electron radiation³⁴ or ion implantation³⁵. Zn interstitials or oxygen vacancies in C doped ZnO (ZnO:C) has also shown to enhance ferromagnetism in pulsed laser deposited films³⁶.

In this work, a detailed study on the preparation of pure $\text{Zn}_{1-x}\text{R}_x\text{O}$ ($\text{R} = \text{Li, Mg, Cr, Mn, Fe and Cd}$) is reported, with constant weight percent of 3% from R ions vs. ZnO. We found that the magnetic properties of ZnO strongly depended on type of R content in ZnO matrix. By controlling the R content, different and unprecedented magnetic properties were reported along with structural, morphological and optical properties. For the *ab initio* calculations we considered direct replacement of the Zn atoms by the dopants and did not consider Zn or O vacancies. While the Li and Cd doped systems remained paramagnetic, the Mg, Cr, Mn and Fe doped systems show ferromagnetism. In the Cr, Mn and Fe-doped systems the presence of d electrons can be held responsible for giving rise to magnetism, but a deeper explanation for the d^0 ferromagnetism in the Mg doped is the scope for future work. However, these properties can be taken advantage of in spintronic applications.

Results and discussion

Structure and XRD

At ambient condition, ZnO has a hexagonal wurtzite structure with lattice parameters a and c equal to ~ 3.25 and ~ 5.20 Å respectively³⁷. In this work, we have substituted 3% of the Zn atoms with Li, Mg, Cr, Fe, Mn and Cd. The crystal structures of the doped systems have been studied using X-ray diffraction (XRD), in order to find any deviation from that of pure ZnO. The XRD patterns of all the systems (pristine and doped) have been shown in Fig. 1.

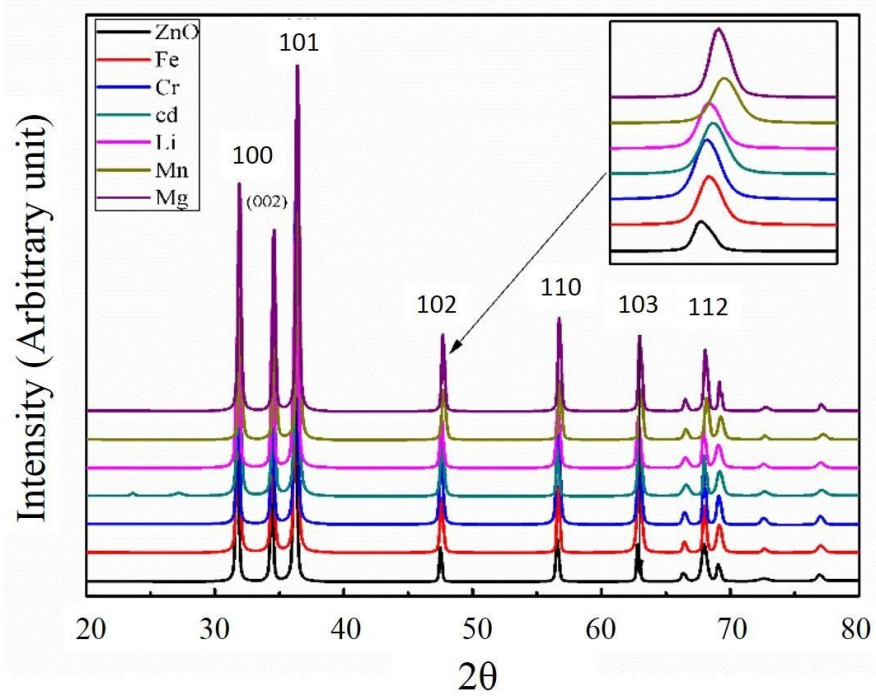


Fig. 1. XRD patterns of pure $\text{Zn}_{1-x}\text{R}_x\text{O}$.

Fig. 1 shows the X-ray diffraction pattern of the $\text{Zn}_{0.97}\text{R}_{0.03}\text{O}$ nanostructure compared to the pure ZnO nanostructure, where (R= Li, Mg, Cr, Mn, Fe and Cd). The pure ZnO has a hexagonal wurtzite structure with a preferred (101) orientation. It is indexed and uses a standard JCPDS file for ZnO (JCPDS 36-1451)) with a preferred (101) orientation. The diffraction peaks correspond to the (002) and (100) planes of ZnO a hexagonal phase in all the samples but with a different intensity ratio. Only the characteristic peaks of ZnO were observed, which confirms that all the synthesized samples are well crystalline, as shown in Fig.1. On the other hand, the peaks slightly shift towards higher angle with doping may be due to the different ionic radii of the dopant ions. The lattice parameters a and c are determined from the following relation,

$$\frac{1}{d_{(hkl)}^2} = \frac{4}{3} \left[\frac{h^2 + hk + k^2}{a^2} \right] + \frac{l^2}{c^2} \quad (1)$$

where h , k and l are the Miller Indices, d is interplanar distance and ' a ' and ' c ' are lattice parameters, and listed in Table (1). Average crystalline size (D) calculated by using

Debye - Scherrer's equation ($D = \frac{k\lambda}{\beta \cos \theta}$) and also listed in Table (1), where $k = 0.94$, a constant, λ is wavelength of X-rays, β is full width at half maximum (FWHM) and θ is the diffraction angle.

Table 1. Crystallite size, lattice strain and lattice parameters of pure ZnO and $\text{Zn}_{0.97}\text{R}_{0.03}\text{O}$ nanoparticles.

$\text{Zn}_{0.97}\text{R}_{0.03}\text{O}$	(D)(nm)	Lattice Strain (ϵ)	$a(\text{\AA})$	$c(\text{\AA})$	c/a
Pure ZnO	43.7	0.241	3.2487	5.2033	1.6017
R= Fe	41.4	0.266	3.251	5.209	1.6023
Cr	41.3	0.225	3.2485	5.21	1.6038
Cd	38.3	0.385	3.25	5.201	1.6003
Li	36.4	0.405	3.254	5.215	1.6026
Mn	35.2	0.351	3.2504	5.2057	1.6016
Mg	35.1	0.352	3.2501	5.2113	1.6034

One can see that the average crystallite size found to decrease with doping. The ionic radii of Zn^{2+} is 0.74 Å while that of Li^{2+} and Mg^{2+} are 0.73 Å and 0.71 Å, respectively for four fold coordination. Zn in ZnO is tetrahedrally coordinated with oxygen. Therefore, the decrement in the lattice size for the Li and Mg substituted ZnO in place of Zn is expected. In order to maintain charge neutrality, Fe and Mn should have valency of 2+. But the ionic radii of Fe^{2+} and Mn^{2+} are 0.77 Å and 0.80 Å, respectively. Therefore, on substituting Zn^{2+} with Fe^{2+} and Mn^{2+} would be expected to increase the lattice size. But from our results, the opposite is seen. Higher valency ions of Fe and Mn have smaller radii than Zn^{2+} . Therefore, it is possible that Fe^{2+} and Fe^{3+} (with ionic radius of 0.63 Å) coexist in $\text{Zn}_{0.97}\text{Fe}_{0.03}\text{O}$, leading to an overall decrement in the crystal size. The same can be inferred for Mn. Mn^{2+} possibly coexists with Mn^{4+} which has an ionic radius of 0.53 Å. Chromium in the four fold coordination can have valencies 4+, 5+ and 6+ and their ionic radii are 25.6%, 34.5% and 45.9% smaller than that of Zn^{2+} . Therefore, the smaller crystal size of $\text{Zn}_{0.97}\text{Cr}_{0.03}\text{O}$ than pure ZnO is justified. However, for the case of Cd, although, Cd^{2+} has a larger ionic radius than Zn^{2+} , the crystal size is found to decrease.

This decrease in the crystallite size may be due to the decrease of nucleation of ZnO nanoparticles by doping with Cd. Also, the slight variation in lattice parameter likely results from the substitution of doped ions with different ionic radii of Zn. Furthermore, it is noted that there is an increase in its lattice strain ($\epsilon = \beta_{hkl} \cos\theta/4$) due to *R*-doping inside the ZnO matrix (Table 1), which causes the local distortion of the crystal structure. This is expected and has been found in previous studies too ³⁸.

HR- TEM and SEM

In order to further check both the average size and shape of our grown samples, we have carried out both High resolution Transmission Electron Microscopy (HR-TEM) (Fig. 2) and Scanning Electron Microscopy (SEM) (Fig. 3). It can be seen from Fig. 2 that the average particle size is about 42 nm. This agrees well with the XRD data analysis. Additionally, the SEM images show a semi-spherical shape of the ZnO sample. The morphology of $\text{Zn}_{0.97}\text{R}_{0.03}\text{O}$ nanoparticles were also studied from SEM image (Fig. 3: a-f). The SEM image represents the agglomeration of particles and also with narrow particle size distribution.

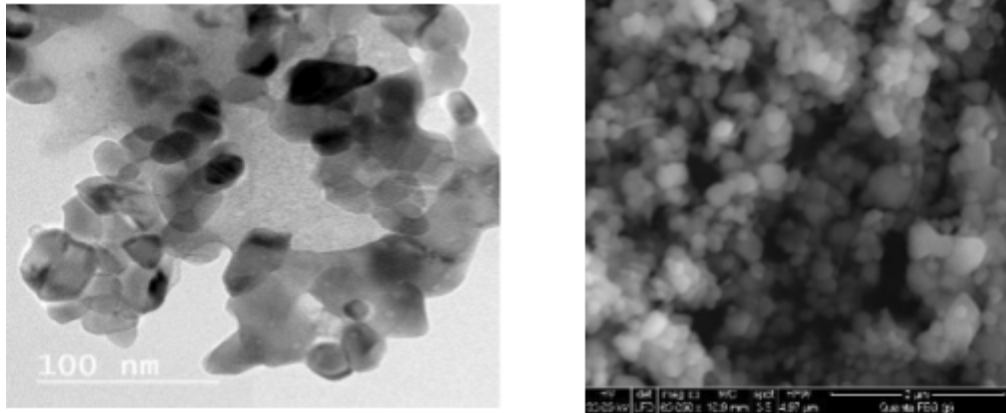


Fig. 2. TEM (left image) and SEM (right image) investigations of the pure ZnO.

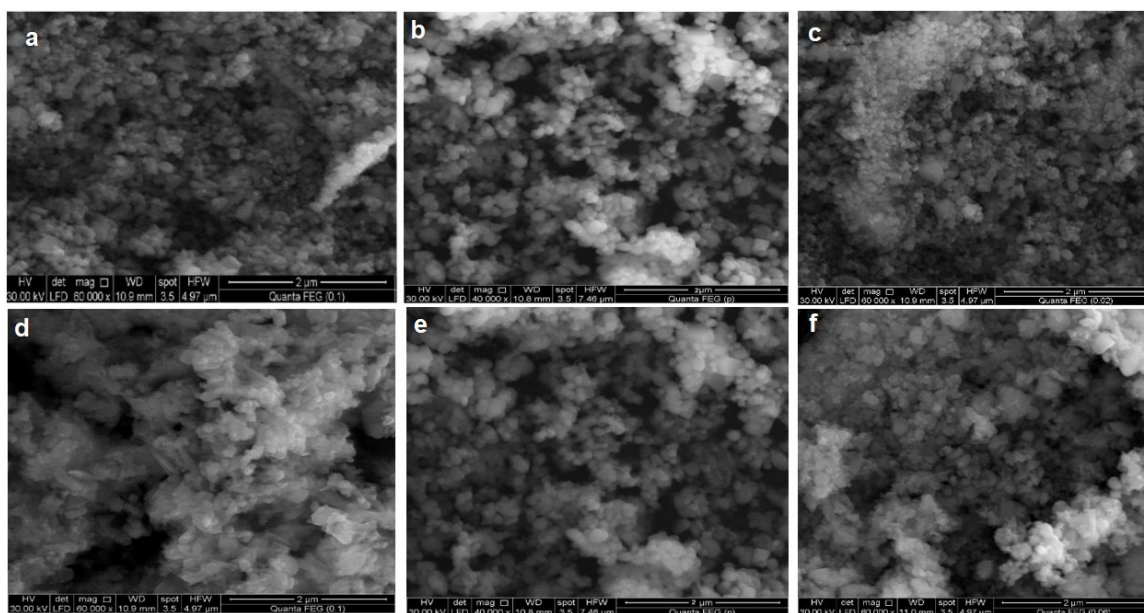


Fig. 3 (a-f). SEM images for $Zn_{1-x}R_xO$ samples, for 3% R concentrations Mn, Cr, Cd, Li, Mg and Fe respectively.

FTIR Spectroscopy

We have performed a Fourier-transform Infrared (FTIR) spectroscopy for all investigated samples to determine the vibrational modes present. Fig. 4 shows the FTIR spectrum of the $Zn_{0.97}R_{0.03}O$ nanoparticles compared to the pure ZnO, where (R = Li, Mg, Cr, Mn, Fe and Cd) synthesized from Zinc Sulfate acquired in the range of $500-4000\text{ cm}^{-1}$ observed at different regions of FTIR spectrum. The observed spectra exhibited well defined absorption peaks in the range of 550 cm^{-1} which is a manifestation of the stretching vibrational mode of ZnO ³⁹. The absorption peak that appears at 3420 cm^{-1} is due to the O–H stretching vibrations of H_2O . The peak around 1636 cm^{-1} is due to the H–O–H bending vibration. These O-H vibrations are present due to a small amount of H_2O in ZnO nanoparticles ⁴⁰. Shoulder peaks are seen to exist around the bands at around 1420 cm^{-1} . These shoulders have an asymmetric stretching of resonance interaction between vibration modes of oxide ions. Furthermore, on doping, no shift in the position of the peaks is observed in the absorption band corresponding to wurtzite ZnO. This is a confirmation of the fact that all the bond stretchings are independent of dopant

concentration and nature. The absence of shifts in vibrational frequencies is independent of the dopant element.

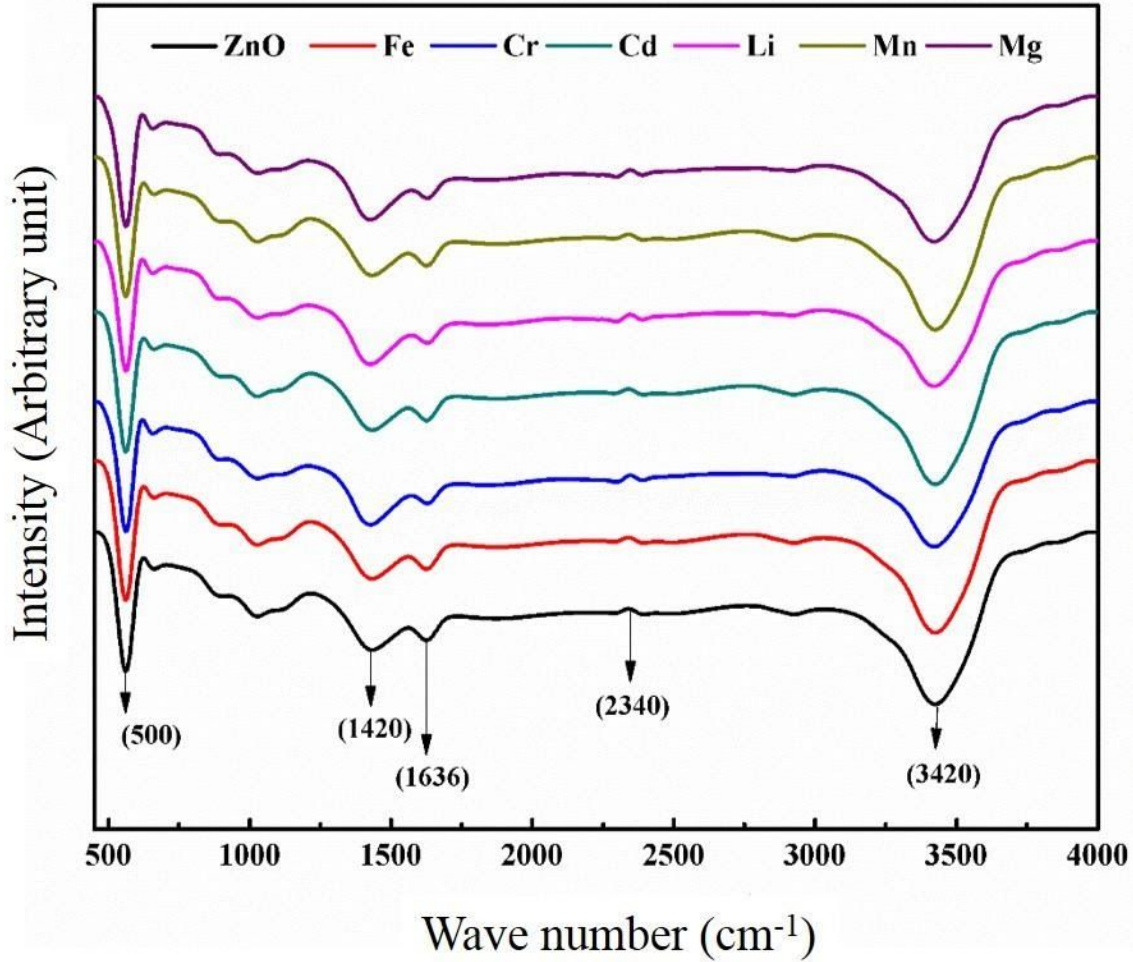


Fig. 4. FTIR spectra of pure ZnO and $\text{Zn}_{0.97}\text{R}_{0.03}\text{O}$ samples.

DFT Calculations

In our calculations, we explored two different atomic positions of the dopants and checked for the minimum energy configuration. In the first configuration, the dopant atoms are separated by one oxygen atom which we designate as ‘near’ (Fig. 5a). In the other configuration, the dopant atoms are separated by $-\text{O}-\text{Zn}-\text{O}-$ and we call this one the ‘far’ configuration (Fig. 5b). We then calculated the minimum energy configuration and did further analysis with those structures.

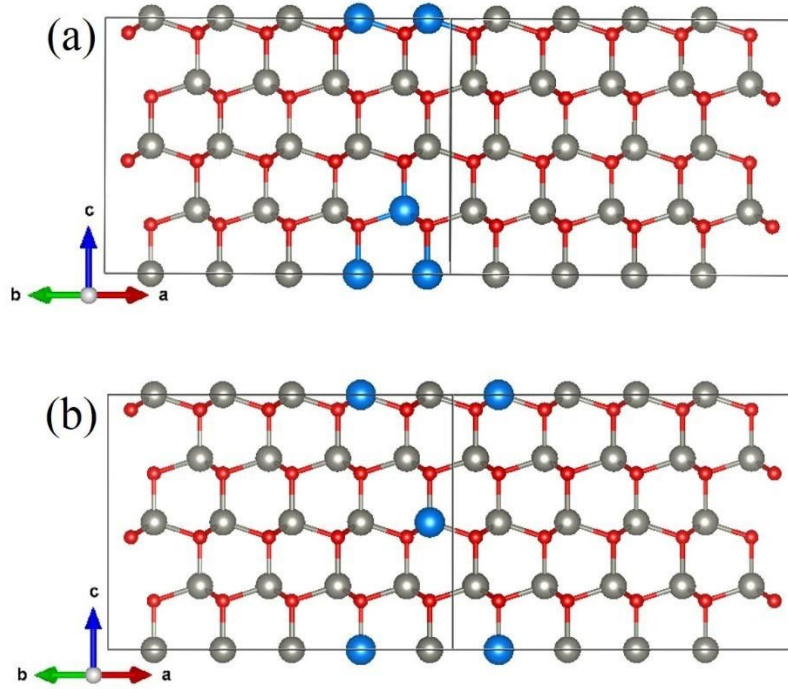


Fig. 5. Wurtzite supercell of ZnO doped with 3% dopant atoms. Dopant atoms are separated by a) an oxygen atom (near) and b) -O-Zn-O- (far). The grey, red and blue atoms represent Zn, O and the dopant atoms respectively.

The energy difference of the two configurations is shown in Fig. 6. It is clear that for Li, Mg and Cd, the far configuration is energetically more favorable. Although, for Mg and Cd the energy differences between the near and far configurations are very small compared to that of Li, we still proceeded with the far configuration for our calculations. For the transition metals, Cr and Fe, the near configuration turns out to be the lower energy structures, while it is opposite for Mn. This trend for Cr, Mn and Fe is in excellent agreement with that obtained by Gopal *et al.*⁴¹. Although, the magnitudes are different from that shown in Ref. 41, this is due to the difference in the dopant concentration and the different pseudopotentials used in our calculations.

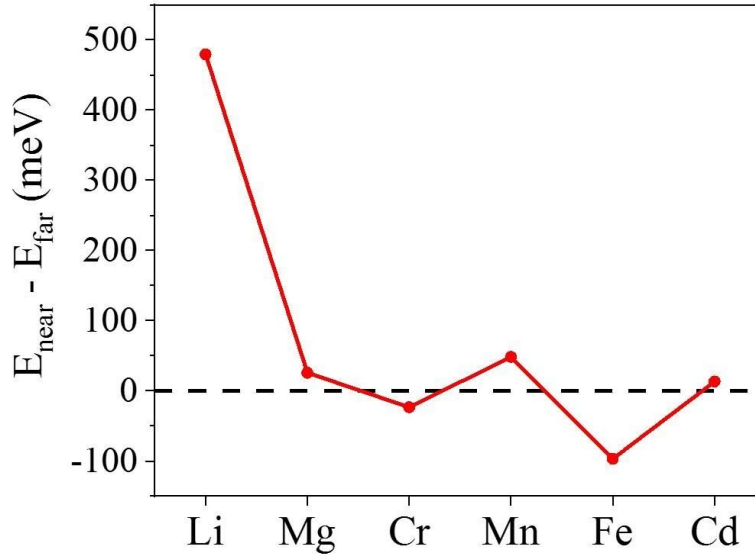


Fig. 6. $E_{\text{near}} - E_{\text{far}}$ for substitutional dopant ions. The negative energy difference indicates that the TM ions prefer to be in a near spatial configuration.

The doped structures were allowed to relax with respect to all the degrees of freedom and eventually, the experimental findings were verified. For all the doped cases, the wurtzite morphology of ZnO is maintained and no structural phase transition is observed. We have even shown this experimentally from our XRD. The structural parameters of all the doped systems is presented in Table 2. The lattice parameters don't show significant differences for the different dopant cases in comparison to the pristine wurtzite ZnO structure. The maximum deviation is seen for Cd. This can be attributed to the larger ionic radii. The almost constant c/a value confirms the consistency of the wurtzite structure. As can be seen, the experimental (Table 1) and calculated (Table 2) data are in very close agreement.

Table 2. Lattice constants and the dopant-oxygen bond length obtained from calculations.

Dopant (3% doping)	Avg. M-O bond length(Å)	a (Å)	c (Å)	c/a
Li	1.965(8)	3.2488(1)	5.2240(1)	1.6079(7)
Mg	1.960(6)	3.2557(1)	5.2251(0)	1.6049(0)
Cr	2.040(5)	3.2597(4)	5.2331(4)	1.6053(8)
Mn	2.012(1)	3.2588(6)	5.2355(3)	1.6065(5)
Fe	1.971(7)	3.2571(7)	5.2352(4)	1.6072(9)
Cd	2.169(2)	3.2635(6)	5.2449(0)	1.6071(1)

With respect to chemical bonding, ZnO is a tricky material as it shows a mixture of both ionic and covalent bonding. The electron transfer from Zn to O is 1.15, which is not strong enough for ionic bonding or not too less for covalent bonding. We calculated the Bader charge transfer (Table 3) using the Atoms in Molecules theory⁴². Amongst, all the doped systems studied in this work, the Zn-O bonds still remain partially covalent and ionic. However, for Li, Mg, Cr, Mn and Fe, the dopant and oxygen bonding tend more towards the ionic side. Given that Zn and Cd belong to the same group elements (d^{10}), the electron transfer from them to oxygen is almost same and therefore for the cadmium doped system, the whole system once again retains both the ionic and covalent traits.

Table 3. Bader charge transfer from Zn and dopant atoms to O.

Dopant (3% doping)	Number of Electrons Donated by Zn to O	Number of Electrons Donated by Dopant to O
Li	1.15	0.84
Mg	1.15	1.63
Cr	1.15	1.35
Mn	1.15	1.33
Fe	1.15	1.31
Cd	1.15	1.13

Experimentally (*vide infra*), we observed that by introducing Cr, Mn and Fe to the ZnO, a clear hysteresis loops being observed and we confirmed the existence of ferromagnetism in these materials. From our calculations, the magnetic moments that were obtained are 3.67, 5.0 and 4.33 μ_B per dopant atom for Cr, Mn and Fe respectively (Fig. 7). These numbers are in very good agreement with previously obtained values ^{43,44}. While Cr and Fe tend to form clusters, Mn has more propensity to remain evenly distributed within the system thus not leading to cluster derived magnetism. As reported by Xing *et al.* the occurrence of ferromagnetism in transition metal-doped ZnO could possibly be due to the increase in the number of defects and oxygen vacancies ⁴⁵. Another opinion according Chu *et al.* is that the exchange interaction between transition metal ions and O ion spin moments can lead to ferromagnetism ⁴⁶.

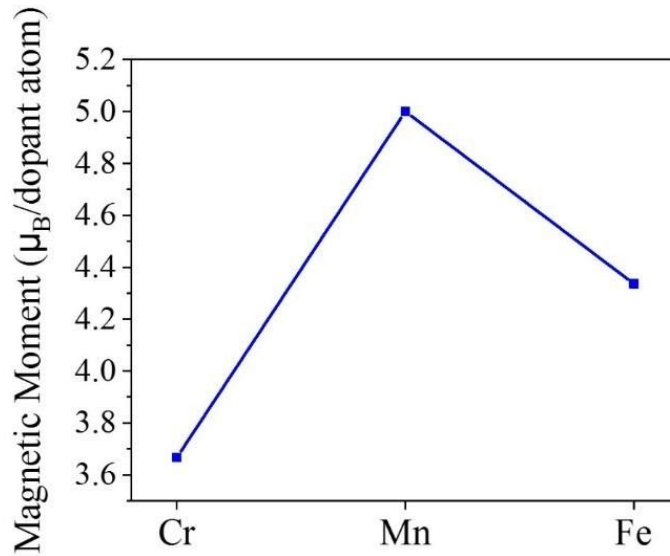


Fig. 7. Magnetic moment per dopant atom.

Magnetic Properties

The temperature dependencies of magnetization zero-field cooling (ZFC) and field cooling (FC) have been shown in Fig. 8 for the doped ZnO samples. A distinct ferromagnetic transition is seen for the Fe/Mn/Cr/Mg-doped sample samples. The ferromagnetic transition temperature (T_c) is accurately estimated from the derivative plot

of magnetization data. Iron doping enhances the ferromagnetism of $\text{Zn}_{1-x}\text{Fe}_x\text{O}$ with the T_c increasing from 39 K for 2% doping to 44 K for 8% doping⁴³. As shown in (Ref. 43) the decrement vanishes upon applying high magnetic field and the ZFC curve overlaps with the FC curve. This downturn is similar to that seen in Ref. 43 and can be attributed to the antiphase ferromagnetic domains.

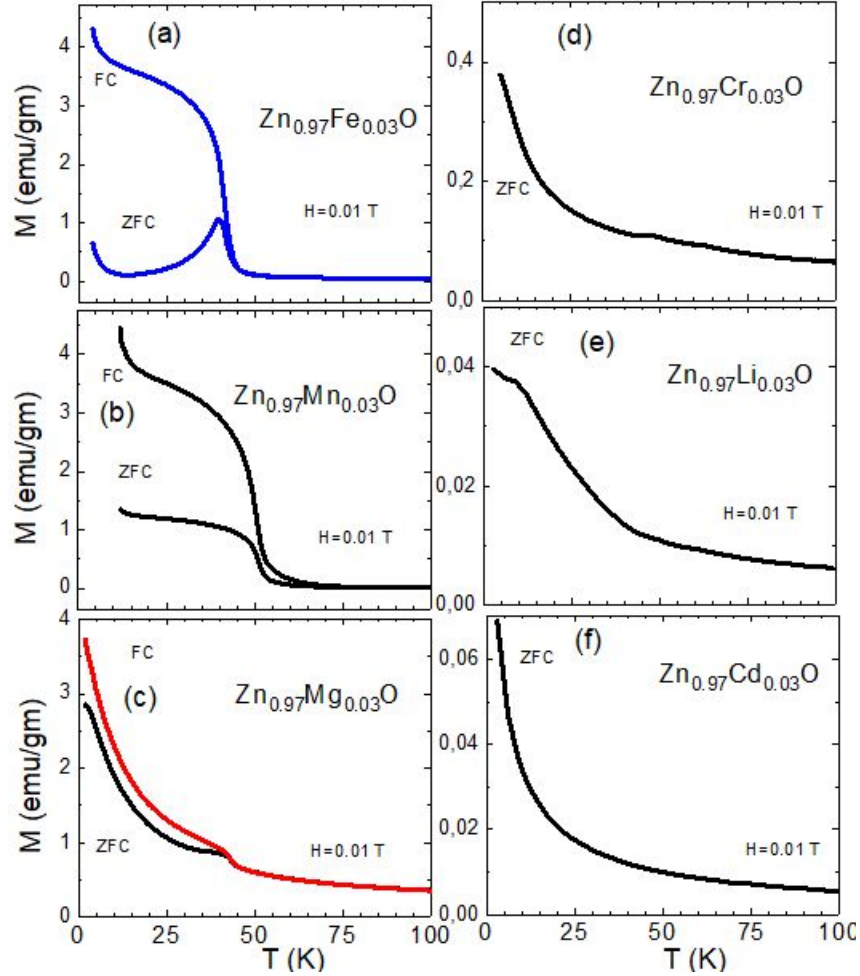


Fig. 8: the temperature dependence of the magnetization (M) in an external field of 0.01T. M has been deduced from the dc magnetization measured by following ZFC and FC protocols.

Effect of doping exhibits a clear magnetic hysteresis loop (Fig.9) for the Mg, Cr, Mn and Fe cases. Mg, Cr, Mn and Fe ions substituting into the ZnO induced weak ferromagnetism and illustrates a magnetic moment without any distortion in the

geometrical symmetry. It is important to note that the reduced moment values might occur due to large disordered spins in the surface as well due to grain boundaries that constitute a considerable fraction of the nano-sample. These vacancies will be ordered in the unique axis of magnetization (c-axis) in our case as the films exhibit hexagonal symmetry.

Importantly, it is well known that undoped ZnO is diamagnetic in nature. Thus, the ferromagnetism observed in our investigated samples is intrinsic and can not be attributed to any kind of defect ⁴⁷. Therefore, ferromagnetism in our investigated samples could be arising from spin-orbit interaction, through *s-d* orbitals coupling ⁴⁸, or interaction between bound magnetic polarons. In the latter case, the fluctuations of magnetization have an important role on both binding and a non-trivial thermal behavior ⁴⁹, thus, the formation of charge carrier quantum states exists on the doped ZnO. However, the interaction between bound magnetic polarons is still an open issue and still up to date there is no direct understanding of the origin of ferromagnetism.

As inferred by Karmakar *et al.* ⁵⁰, native defects in ZnO host can give rise to ferromagnetism in TM-doped ZnO system. According to Jin *et al.* ⁵¹, the bound magnetic polaron (BMP) model can be applied to explain room temperature ferromagnetism. The BMP model puts forward the idea that the long-range ordering is either due to the direct overlaps between BMPs or indirect interactions between the BMPs and magnetic impurity. Thus, doping with Cr increases the density of magnetic impurities, facilitating the ferromagnetic alignment of BMPs. It has also been proposed in literature ⁵² that the spin polarized carriers and the hybridization between the O-p and TM-d orbitals may be responsible for the ferromagnetism in Cr-doped ZnO. From our calculations the average magnetic moment of Cr atom is found to be about 3.65 μ_B /Cr. This value is much larger than our experimental data. The reason behind this discrepancy can be explained as follows. The processes of film preparation is often a non-equilibrium process. During the process, Cr atoms may get embedded in the antiferromagnetic far state which does not contribute to the ferromagnetism. Although, it is widely proposed that defects, Zn or O vacancies along with the presence of magnetic dopants also play a crucial role in the

enhancement or suppression of ferromagnetism ^{53–60}. However, in our calculations, the simplest cases have been treated with only replacement of Zn atoms by the dopants.

In the absence of magnetic impurities, exchange interactions between localized electron spin moments resulting from oxygen vacancies at the surfaces of nanoparticles can be the cause of ferromagnetism. A common consensus with regards to the ferromagnetic property in transition-metal-doped ZnO is that defects such as oxygen or zinc vacancies might be responsible ^{61–63}. It has already been shown that oxygen vacancy is crucial for Mn doped In_2O_3 ⁶⁴. Although, the reason behind the intrinsic ferromagnetism in Mn-doped oxides is still not completely understood, it is believed that defects do play a role in the origin of the ferromagnetism in the Mn-doped ZnO system. The theoretical work by Gopal *et al.* shows that in TM-doped ZnO and particularly Co-doped ZnO, the defects do favor ferromagnetic states ⁴¹. This makes the claim for Mn-doped ZnO stronger. Finally, the diamagnetic dilution in the hexagonal diamagnetic lattice films of wurtzite structure resulted in improved values of magnetic moment and ferromagnetic character which needs further investigations in our future work. We believe that for the case of Mg in our work, it is defects such as Zn and O vacancies which give rise to the d^0 ferromagnetism. From our theoretical calculations, we did not consider any defects (V_{Zn} or O_{Zn}) in the lattice and did not also find any ferromagnetic moment for the Mg doped case. In general, the occurrence and improvement in the ferromagnetic behavior is also dependent on the synthesis route.

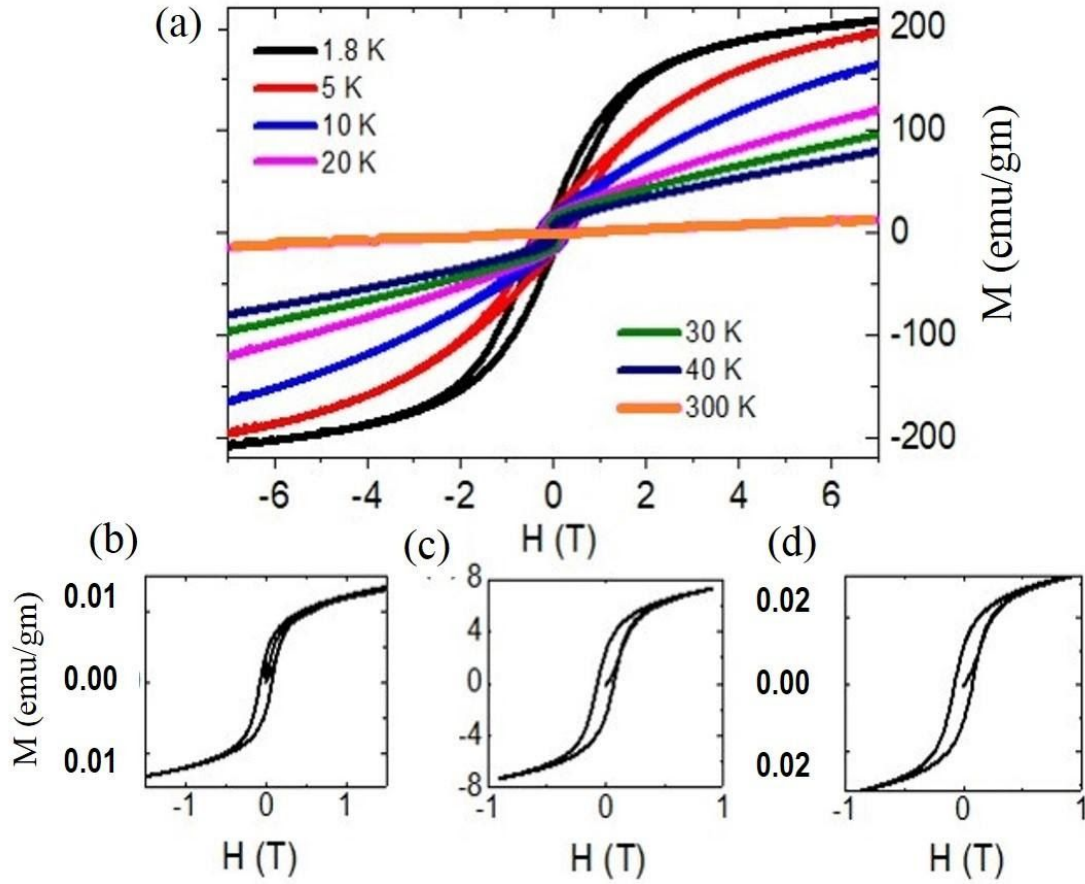


Fig.9: (a-d) show the isothermal magnetization M vs. H loops of $\text{Zn}_{0.97}\text{R}_{0.03}\text{O}$ [$\text{R}=\text{Fe}$ (a), Mn (b), Mg (c), Cr (d)] measured at different temperatures in (a) ranging from 1.8 to 300K up to 7T. From (b-d) the isothermal magnetization M vs. H being collected at 300K.

Conclusion

In summary, pure and metal (Li, Mg, Cr, Mn, Fe and Cd)-doped ZnO nanoparticles were successfully synthesized. The original hexagonal wurtzite structure ($P6_3mc$) was retained. For none of the doped cases any structural phase transition was observed. The pure ZnO revealed paramagnetic trend as expected, but the Fe, Mn, Mg, and Cr doping induced ferromagnetism at different levels. The spatial configuration of the dopant atoms is determined theoretically, giving a better understanding of the dopant atom orientation responsible for magnetism. The Fe and Cr atoms tend to form clusters giving rise to ferromagnetism while the Mn atoms remain more spread out. Several reasons behind the observed ferromagnetism have been discussed. Specifically, the role of defects has been

emphasized behind the ferromagnetism obtained. This is further strengthened by the case of the Mg (non-magnetic) doped case, where the formation of defects in the system can give the best justification for the occurrence of ferromagnetism.

Experimental and Theoretical Methods

All the gradual steps leading to the preparation (weighing, mixing, grinding, and storage) were carried out in an Ar-filled glove box. Both the O₂ and H₂O levels were kept at less than 0.1 ppm. The preparation of Zn_{1-x}R_xO where (x = 0.03) in a nanoparticle form has been achieved by using the co-precipitation method. The following procedure was adopted. Zinc sulfate (ZnSO₄) and NaOH solutions were prepared separately and then eventually mixed together. This mixed solution was maintained at room temperature and stirred for 2 hours. For drying purposes, the Zn(OH)₂ was heated at 70 °C for 24. The dried ingots were heated at 400 °C for 4 hours. Then the powder was left to cool down slowly to room temperature to get pure zinc oxide (ZnO). In order to prepare mixed oxide dilute magnetic semiconductors, mixed solutions of ZnSO₄ and the metal(R) sulfate at the desired ratio were prepared. Finally, NaOH solution was added slowly to the mixed solution. This process described, was repeated to obtain Zn_{0.97}R_{0.03}O nanoparticles for the different metals considered (R = Li, Mg, Cr, Mn, Fe and Cd).

All the structures including the pristine and doped ones were relaxed within the framework of Density Functional Theory (DFT) ⁶⁵ by solving the Kohn-Sham equations ⁶⁶. Our total energy and electronic structure calculations were performed using the projector augmented wave (PAW) ⁶⁷ formalism of density functional theory as implemented in the VASP package ⁶⁸. We used a well-converged energy cutoff of 550 eV and the Brillouin zone was sampled employing a 2 × 2 × 3 Monkhorst-Pack k-point mesh ⁶⁹. The Zn, O, Li, Mg, Cr, Mn, Fe and Cd potentials were employed with valence states of 3d¹⁰4s², 2s²2p⁴, 2s¹, 3s², 3p⁶3d⁵4s¹, 3d⁶4s¹, 3p⁶3d⁵4s¹ and 4d¹⁰5s², utilizing the Perdew-Burke-Ernzerhof (PBE) exchange correlation functional ⁷⁰. All the structures were relaxed until the Hellmann-Feynman forces were less than 0.05 eV/Å. Typically,

standard DFT calculations tend to grossly underestimate the electronic band gap of wide gap insulators or even semiconductors containing transition-metals. Therefore, a Hubbard parameter (U) is included to account for the d - d Coulomb interaction^{71–73}. In order to add the on-site d - d Coulomb interaction, U , and the on-site exchange interaction, J , to the generalized gradient approximation (GGA) Hamiltonian for transition-metal elements, we use a typical value of $U-J = 4.0$ eV for our calculations that contain transition metals, *i.e.* Cr, Fe and Mn. In order to mimic the experimental doping concentration, we constructed a periodic $5 \times 5 \times 2$ supercell of ZnO containing 200 atoms (100 Zn and 100 O atoms). Since, in the experiments, the doping concentration was 3%, in our calculations we replaced 3 of the Zn atoms with the dopant atoms.

References

1. Dietl, T., Ohno, H., Matsukara, F., Cibert, J. & D, F. Zener Model Description of Ferromagnetism in Zinc-Blende. *Science* **287**, 1019–1023 (2000).
2. Hachimi, A. G. El, Zaari, H., Benyoussef, A., Yadari, M. El & Kenz, A. El. First-principles prediction of the magnetism of 4f rare-earth-metal-doped wurtzite zinc oxide. *J. Rare Earths* **32**, 715–721 (2014).
3. Zhang, M. *et al.* Transition Metal Adsorbed-Doped ZnO Monolayer : 2D Dilute Magnetic Semiconductor , Magnetic Mechanism , and Beyond 2D. *ACS Omega* **2**, 1192–1197 (2017).
4. Ahmed, S. A. Room-temperature ferromagnetism in Co- , Cr- , and V-doped ZnO diluted magnetic semiconductor. *Appl. Phys. A* **123**, 440 (2017).
5. Jin, Z. *et al.* High throughput fabrication of transition- metal-doped epitaxial ZnO thin films : A series of oxide-diluted magnetic semiconductors and their properties. *Appl. Phys. Lett.* **78**, 3824–3826 (2001).
6. Zheng, J. H., Song, J. L., Zhao, Z., Jiang, Q. & Lian, J. S. Optical and magnetic properties of Nd-doped ZnO nanoparticles. *Cryst. Res. Technol.* **47**, 713–718 (2012).
7. Mounkachi, O. *et al.* Magnetic properties of $\text{Zn}_{0.9}(\text{Mn}_{0.05}\text{Ni}_{0.05})\text{O}$ nanoparticle:

- Experimental and theoretical investigation. *J. Magn. Magn. Mater.* **324**, 1945–1947 (2012).
8. Mounkachi, O., Benyoussef, A., Kenz, A. El, Saidi, E. H. & Hill, E. K. Electronic structure of acceptor defects in (Zn , Mn) O and (Zn , Mn)(O , N). *J. Appl. Phys.* **106**, 093905 (2209).
 9. Gong, H., Hu, J. Q., Wang, J. H., Ong, C. H. & Zhu, F. R. Nano-crystalline Cu-doped ZnO thin film gas sensor for CO. *Sensors Actuators B* **115**, 247–251 (2006).
 10. Yodyingyong, S. *et al.* ZnO nanoparticles and nanowire array hybrid photoanodes for dye-sensitized solar cells. *Appl. Phys. Lett.* **96**, 073115 (2010).
 11. Zheng, M. J., Zhang, L. D., Li, G. H. & Shen, W. Z. Fabrication and optical properties of large-scale uniform zinc oxide nanowire arrays by one-step electrochemical deposition technique. *Chem. Phys. Lett.* **363**, 123–128 (2002).
 12. Adams, L. K., Lyon, D. Y. & Alvarez, P. J. J. Comparative eco-toxicity of nanoscale TiO₂, SiO₂, and ZnO water suspensions. *Water Res.* **40**, 3527–3532 (2006).
 13. Nunes, P. *et al.* Effect of different dopant elements on the properties of ZnO thin films. *Vacuum* **64**, 281–285 (2002).
 14. Panwar, A. & Yadav, K. L. A novel one-pot synthesis of hierarchical europium doped ZnO nanoflowers. *Mater. Lett.* **142**, 30–34 (2015).
 15. More, D. *et al.* Correlation of structural and magnetic properties of Ni-doped ZnO nanocrystals. *J. Phys. D. Appl. Phys.* **47**, 045308 (2014).
 16. Pearton, S. J., Heo, W. H., Ivill, M., Norton, D. P. & Steiner, T. Dilute magnetic semiconducting oxides. *Semicond. Sci. Technol. Top.* **19**, R59–R74 (2004).
 17. Zutic, I., Fabian, J. & Sarma, S. Das. Spintronics: Fundamentals and applications. *Rev. Mod. Phys.* **76**, 323–410 (2004).
 18. Li, Q. *et al.* Photoluminescence and wetting behavior of ZnO nanoparticles / nanorods array synthesized by thermal evaporation. *J. Alloys Compd.* **560**, 156–160 (2013).

19. Hu, P., Han, N., Zhang, D., Ho, J. C. & Chen, Y. Chemical Highly formaldehyde-sensitive, transition-metal doped ZnO nanorods prepared by plasma-enhanced chemical vapor deposition. *Sensors Actuators B. Chem.* **169**, 74–80 (2012).
20. Shi, R., Yang, P., Dong, X., Ma, Q. & Zhang, A. Growth of flower-like ZnO on ZnO nanorod arrays created on zinc substrate through low-temperature hydrothermal synthesis. *Appl. Surf. Sci.* **264**, 162–170 (2013).
21. Coey, J. M. D., Venkatesan, M. & Fitzgerald, C. B. Donor impurity band exchange in dilute ferromagnetic oxides. *Nat. Mater.* **4**, 173–179 (2005).
22. Coey, J. M. D., Wongsaprom, K., Alaria, J. & Venkatesan, M. Charge-transfer ferromagnetism in oxide nanoparticles. *J. Phys. D. Appl. Phys.* **41**, 134012 (2008).
23. Coey, J. M. D., Stamenov, P., Gunning, R. D., Venkatesan, M. & Paul, K. Ferromagnetism in defect-ridden oxides and related materials. *New J. Phys.* **12**, 053025 (2010).
24. Motaung, D. E. *et al.* Shape-Selective Dependence of Room Temperature Ferromagnetism Induced by Hierarchical ZnO Nanostructures. *ACS Appl. Mater. Interfaces* **6**, 8981–8995 (2014).
25. Beltran, J. J., Barrero, C. A. & Punnoose, A. Understanding the role of iron in the magnetism of Fe doped ZnO nanoparticles. *Phys. Chem. Chem. Phys.* **17**, 15284–15296 (2015).
26. Xu, X. *et al.* Size Dependence of Defect-Induced Room Temperature Ferromagnetism in Undoped ZnO Nanoparticles. *J. Phys. Chem. C* **116**, 8813–8818 (2012).
27. Sanchez, N., Gallego, S., Cerdá, J. & Muñoz, M. C. Tuning surface metallicity and ferromagnetism by hydrogen adsorption at the polar ZnO (0001) surface. *Phys. Rev. B* **81**, 115301 (2010).
28. Schoenhalz, A. L., Arantes, J. T., Fazzio, A. & Dalpian, G. M. Surface magnetization in non-doped ZnO nanostructures. *Appl. Phys. Lett.* **94**, 162503 (2009).

29. Zhan, P. *et al.* Origin of the defects-induced ferromagnetism in un-doped ZnO single crystals. *Appl. Phys. Lett.* **102**, 071914 (2013).
30. Lany, S., Osorio-guillén, J. & Zunger, A. Origins of the doping asymmetry in oxides: Hole doping in NiO versus electron doping in ZnO. *Phys. Rev. B* **75**, 241203 (2007).
31. Pan, H. *et al.* Room-Temperature Ferromagnetism in Carbon-Doped ZnO. *Phys. Rev. Lett.* **99**, 127201 (2007).
32. Elfimov, I. S. *et al.* Magnetizing Oxides by Substituting Nitrogen for Oxygen. *Phys. Rev. Lett.* **98**, 137202 (2007).
33. Coey, J. M. D. d0 ferromagnetism. *Solid State Sci.* **7**, 660–667 (2005).
34. Vlasenko, L. S. & Watkins, G. D. Optical detection of electron paramagnetic resonance for intrinsic defects produced in ZnO by 2.5-MeV electron irradiation in situ at 4.2 K. *Phys. Rev. B* **72**, 035203 (2005).
35. Kucheyev, S. O., Williams, J. S. & Jagadish, C. Ion-beam-defect processes in group-III nitrides and ZnO. *Vacuum* **73**, 93–104 (2004).
36. Li, X., Guo, J., Quan, Z., Xu, X. & Gehring, G. A. Defects Inducing Ferromagnetism in Carbon-Doped ZnO Films. *IEEE Trans. Magn.* **46**, 1382–1384 (2010).
37. Albertsson, J., Abrahams, S. C. & Kvik, A. Atomic Displacement, Anharmonic Thermal Vibration, Expansivity and Pyroelectric Coefficient Thermal Dependences in ZnO. *Acta Crystallogr.* **B45**, 34–40 (1989).
38. Irshad, K., Tahir, M. & Murtaza, A. Synthesis and characterization of transition-metals-doped ZnO nanoparticles by sol-gel auto-combustion method. *Phys. B Phys. Condens. Matter* **543**, 1–6 (2018).
39. Bhatia, S., Verma, N. & Bedi, R. K. Ethanol gas sensor based upon ZnO nanoparticles prepared by different techniques. *Results Phys.* **7**, 801–806 (2017).
40. Kaneva, N. V & Dushkin, C. D. Preparation of nanocrystalline thin films of ZnO by sol-gel dip coating. *Bulg. Chem. Commun.* **43**, 259–263 (2011).
41. Gopal, P. & Spaldin, N. A. Magnetic interactions in transition-metal-doped ZnO :

- An ab initio study. *Phys. Rev. B* **74**, 094418 (2006).
42. Henkelman, G., Arnaldsson, A. & Jonsson, H. A fast and robust algorithm for Bader decomposition of charge density. *Comput. Mater. Sci.* **36**, 354–360 (2006).
 43. Abdel-Baset, T. A., Fang, Y., Anis, B., Duan, C. & Abdel-hafiez, M. Structural and Magnetic Properties of Transition-Metal-Doped Zn $1 - x$ Fe x O. *Nanoscale Res. Lett.* **11**, 115 (2016) and IA Abdel-Latif, I. Hassen, A. Zybilla, C. Abdel-Hafiez, M. Allam, S. El-Sherbini, Th. *Journal of alloys and compounds* **452**, 245-248 (2008)
 44. Abdel-Baset, T. A., Fang, Y., Duan, C. & Abdel-hafiez, M. Magnetic Properties of Chromium-Doped ZnO. *J. Supercond. Nov. Magn.* **29**, 1937–1942 (2016) and Arango, YC. Vavilova, E. Abdel-Hafiez, M. et al., *Physical Review B* **84**, 134430 (2011).
 45. Xing, G. Z. *et al.* Strong correlation between ferromagnetism and oxygen deficiency in Cr-doped $\text{In}_2\text{O}_{3-\delta}$ nanostructures. *Phys. Rev. B* **79**, 174406 (2009).
 46. Chu, D., Zeng, Y. & Jiang, D. Synthesis and growth mechanism of Cr-doped ZnO single-crystalline nanowires. *Solid State Commun.* **143**, 308–312 (2007).
 47. Wang, Q., Sun, Q., Chen, G., Kawazoe, Y. & Jena, P. Vacancy-induced magnetism in ZnO thin films and nanowires. *Phys. Rev. B* **77**, 205411 (2008).
 48. Beuneu, F. & Monod, P. The Elliott relation in pnre metals. *Phys. Rev. B* **18**, 2422–2425 (1978).
 49. Natali, F. *et al.* Role of magnetic polarons in ferromagnetic GdN. *Phys. Rev. B* **035202**, 035202 (2013).
 50. Karmakar, D. *et al.* Ferromagnetism in Fe-doped ZnO nanocrystals: Experiment and theory. *Phys. Rev. B* **75**, 144404 (2007).
 51. Jin, C. G. *et al.* Tunable ferromagnetic behavior in Cr doped ZnO nanorod arrays through defect engineering. *J. Mater. Chem. C* **2**, 2992–2997 (2014).
 52. Li, L. *et al.* Ferromagnetism in polycrystalline Cr-doped ZnO films : Experiment and theory. *Solid State Commun.* **146**, 420–424 (2008).
 53. Hou, Q., Xu, Z., Jia, X. & Zhao, C. Effects of Ni doping and native point defects

- on magnetism of ZnO first-principles study. *J. Appl. Phys.* **123**, 055106 (2018).
54. Weng, Z. Z., Huang, Z. G. & Lin, W. X. Magnetism of Cr-doped ZnO with intrinsic defects. *J. Appl. Phys.* **111**, 113915 (2012).
 55. Weyer, G. *et al.* Defect-related local magnetism at dilute Fe atoms in ion-implanted ZnO. *J. Appl. Phys.* **102**, 113915 (2010).
 56. Ivanovski, V. N. *et al.* A study of defect structures in Fe-alloyed ZnO: Morphology, magnetism, and hyperfine interactions. *J. Appl. Phys.* **126**, 125703 (2019).
 57. Deng, B., Guo, Z. & Sun, H. Theoretical study of Fe-doped -type ZnO. *Appl. Phys. Lett.* **96**, 172106 (2010).
 58. Liu, E.-Z. & Jiang, J. Z. O-vacancy-mediated spin-spin interaction in Co-doped ZnO: First-principles total-energy calculations. *J. Appl. Phys.* **107**, 023909 (2010).
 59. Liu, H. *et al.* Structural , optical and magnetic properties of Cu and V co-doped ZnO nanoparticles. *Phys. E Low-dimensional Syst. Nanostructures* **47**, 1–5 (2013).
 60. Jug, K. & Tikhomirov, V. A. Comparative Studies of Cation Doping of ZnO with Mn, Fe, and Co. *J. Phys. Chem. A* **113**, 11651–11655 (2009).
 61. Li, Y. *et al.* Micro-Brillouin scattering from a single isolated nanosphere. *Appl. Phys. Lett.* **88**, 023112 (2006).
 62. Cong, C. J., Hong, J. H. & Zhang, K. L. Effect of atmosphere on the magnetic properties of the Co-doped ZnO magnetic semiconductors. *Mater. Chem. Phys.* **113**, 435–440 (2009).
 63. Xiong, Z. *et al.* Oxygen enhanced ferromagnetism in Cr- doped ZnO films. *Appl. Phys. Lett.* **99**, 052513 (2011).
 64. An, Y., Wang, S., Duan, L., Liu, J. & Wu, Z. Local Mn structure and room temperature ferromagnetism in Mn-doped In₂O₃ films. *Appl. Phys. Lett.* **102**, 212411 (2013).
 65. Hohenberg, P. & Kohn, W. Inhomogeneous Electron Gas. *Phys. Rev.* **136**, B864 (1964).
 66. Kohn, W. & Sham, L. J. Self-Consistent Equations Including Exchange and

- Correlation Effects. *Phys. Rev.* **140**, A1133 (1965).
67. Blochl, P. E. Projector-Augmented Plane-Wave Method. *Phys. Rev. B* **50**, 17953–18979 (1994).
 68. Kresse, G. & Hafner, J. Ab initio molecular dynamics for liquid metlas. *Phys. Rev. B* **47**, 558–561 (1993).
 69. Monkhorst, H. J. & Pack, J. D. Special points for Brillonin-zone integrations. *Phys. Rev. B* **13**, 5188–5192 (1976).
 70. Perdew, J. P., Burke, K. & Ernzerhof, M. Generalized Gradient Approximation Made Simple. *Phys. Rev. Lett.* **77**, 3865–3868 (1996).
 71. Anisimov, V. I., Zaanen, J. & Andersen, O. K. Band theory and Mott insulators: Hubbard U instead of Stoner I. *Phys. Rev. B* **44**, 943–954 (1991).
 72. Pickett, W. E., Erwin, S. C. & Ethridge, E. C. Reformulation of the LDA \square U method for a local-orbital basis. *Phys. Rev. B* **58**, 1201–1209 (1998).
 73. Cococcioni, M. & Gironcoli, S. De. Linear response approach to the calculation of the effective interaction parameters in the LDA+ U method. *Phys. Rev. B* **71**, 035105 (2005).

Acknowledgements

We thank C. Krellner and R. Klingeler for discussions. A.M and R.A would like to acknowledge the support from Carl Tryggers Stiftelse for Vetenskaplig Forskning (CTS) and the Swedish Research Council (VR). SNIC and HPC2N are also acknowledged for providing computing time. This work has been supported by the Ministry of Education and Science of the Russian Federation in the framework of Increase Competitiveness Program of NUST “MISiS” Grant No. K2-2017-084; by Act 211 of the Government of Russian Federation, Contracts 02.A03.21.0004, 02.A03.21.0006 and 02.A03.21.0011.

Author contributions

T.A.A and M.A performed all the experiments. A.M carried out the first principles calculations. T.A.A, A.M, R.A, A.N.V and M.A designed the work and wrote the manuscript.

Competing interests

The author(s) declare no competing interests.

Figure legends

Figure 1. XRD patterns of pure $\text{Zn}_{1-x}\text{R}_x\text{O}$.

Figure 2. TEM (left image) and SEM (right image) investigations of the pure ZnO.

Figure 3 (a-f). SEM images for $\text{Zn}_{1-x}\text{R}_x\text{O}$ samples, for 3% R concentrations Mn, Cr, Cd, Li, Mg and Fe respectively.

Figure 4. FTIR spectra of pure ZnO and $\text{Zn}_{0.97}\text{R}_{0.03}\text{O}$ samples.

Figure 5. Wurtzite supercell of ZnO doped with 3% dopant atoms. Dopant atoms are separated by a) an oxygen atom (near) and b) $-\text{O}-\text{Zn}-\text{O}-$ (far). The grey, red and blue atoms represents Zn, O and the dopant atoms respectively.

Figure 6. $E_{\text{near}} - E_{\text{far}}$ for substitutional dopant ions. The negative energy difference indicates that the TM ions prefer to be in a near spatial configuration.

Figure 7. Magnetic moment per dopant atom.

Figure 8. Temperature dependence of the magnetization (M) in an external field of 0.01T. M has been deduced from the dc magnetization measured by following ZFC and FC protocols.

Figure 9. (a-d) show the isothermal magnetization M vs. H loops of $\text{Zn}_{0.97}\text{R}_{0.03}\text{O}$ [R=Fe (a), Mn(b), Mg(c), Cr(d)] measured at different temperatures in (a) ranging from 1.8 to 300K up to 7T. From (b-d) the isothermal magnetization M vs. H being collected at 300K.

Table captions

Table 1. Crystallite size, lattice strain and lattice parameters of pure ZnO and $\text{Zn}_{0.97}\text{R}_{0.03}\text{O}$ nanoparticles.

Table 2. Lattice constants and the dopant-oxygen bond length obtained from calculations.

Table 3. Bader charge transfer from Zn and dopant atoms to O.